ARTICLES
https://doi.org/10.1038/s41567-020-0790-3

nature physics

Check for updates

Plasma stopping-power measurements reveal transition from non-degenerate to degenerate plasmas

A. C. Hayes [1]✉, M. E. Gooden [1], E. Henry [2], Gerard Jungman [1], J. B. Wilhelmy [1], R. S. Rundberg [1], C. Yeamans [2], G. Kyrala [1], C. Cerjan [2], D. L. Danielson [1], Jérôme Daligault [1], C. Wilburn [1], P. Volegov [1], C. Wilde [1], S. Batha [1], T. Bredeweg [1], J. L. Kline [1], G. P. Grim [2], E. P. Hartouni [2], D. Shaughnessy [2], C. Velsko [2], W. S. Cassata [2], K. Moody [2], L. F. Berzak Hopkins [2], D. Hinkel [2], T. Döppner [2], S. Le Pape [2], F. Graziani [2], D. A. Callahan [2], O. A. Hurricane [2] and D. Schneider [2]

Physically realized electron gas systems usually reside in either the quantum non-degenerate or fully degenerate limit, where the average de Broglie wavelength of the thermal electrons becomes comparable with the interparticle distance between electrons. A few systems, such as young brown dwarfs and the cold dense fuels created in imploded cryogenic capsules at the National Ignition Facility, lie between these two limits and are partially degenerate. The National Ignition Facility has the unique capability of varying the electron quantum degeneracy by adjusting the laser drive used to implode the capsules. This allows experimental studies of the effects of the degeneracy level on plasma transport properties. By measuring rare nuclear reactions in these cold dense fuels, we show that the electron stopping power, which is the rate of energy loss per unit distance travelled by a charged particle, changes with increasing electron density. We observe a quantum-induced shift in the peak of the stopping power using diagnostics that measure above and below this peak. The observed changes in the stopping power are shown to be unique to the transition region between non-degenerate and degenerate plasmas. Our results support the screening models applied to partially degenerate astrophysical systems such as young brown dwarfs.

As the density of a plasma increases, or the temperature decreases, the system enters a regime where the average de Broglie wavelength of the thermal electrons becomes comparable with the interparticle distance between electrons. This transition to quantum degeneracy results in changes in the physical properties of the plasma, including changes in the electron screening of reaction rates, the stopping power, the viscosity, the thermal and electrical conductivity and the electron–ion equilibration times[1–9]. In astrophysics, main sequence stars fall in the non-degenerate regime[10], while white dwarfs and neutron stars are well described[11,12] by the fully degenerate limit. The properties of fully degenerate electron gases have also been studied in detail in condensed-matter physics, particularly for electron gases in metals[13]. However, the behaviour of plasmas or astrophysical systems in the transition region between the non-degenerate and degenerate quantum limits is considerably less well studied. This is because creating experimentally accessible systems, in which the degree of degeneracy can be varied between the two limits, is very challenging. One class of systems in the cosmos that spans the quantum degeneracy transition regime is astrophysical brown dwarfs, particularly those with masses of about $0.05M_{\odot}$, where $M_{\odot}$ is the mass of the Sun, and with lifetimes less than a billion years[14]. The cold fuels in cryogenic capsules[15] at the National Ignition Facility (NIF)[16] are terrestrial systems spanning a similar degeneracy regime. Although very different in size and origin, these two systems involve similar ranges in temperature and density, for some masses and ages of brown dwarfs (Fig. 1).

The current work focuses on experiments designed to measure changes in plasma transport properties with increasing electron degeneracy. In particular, we focus on changes in the plasma stopping power, which is the rate of energy loss per unit distance travelled by a charged particle. The underlying physics of stopping power has been investigated using several theoretical techniques[4,7,17]. In all cases, it is found that the gross shape of the stopping power is largely determined by kinematics and peaks when the velocity of the moving charged particle (the projectile) is close to the average electron velocity of the plasma, $v_p \approx v_{avg}$. At higher projectile velocities, there are fewer plasma electrons with velocities close to v_p, which reduces the probability of a significant projectile–electron interaction, and results in a lower stopping power. The plasma electron velocity distribution directly affects the shape of the stopping curve, so that dE/dx becomes dependent on the degeneracy of the system. As the density increases, the average electron velocity transitions from a function purely of the electron temperature, $\sqrt{2\theta_e/m_e}$ in the case of non-degenerate plasmas, to a function purely of the electron density such that the average velocity is proportional to the Fermi velocity, $\sqrt{2E_F/m_e}$, in the fully degenerate limit. For partially degenerate plasmas, the average electron velocity is a function of both temperature and density, and this is the regime relevant to the present NIF experiments. Thus, relative to the velocity of the moving charged particle, the peak of the stopping power, or the Bragg peak, shifts as the degree of degeneracy increases.

Degeneracy also affects plasma stopping through a change in the Coulomb logarithm, which incorporates effects due to charge screening and is, therefore, a function of both the average velocity and the dynamic Debye radius. Both the velocity distribution and density of electrons in the Debye sphere are affected. The degeneracy-induced

[1]Los Alamos National Laboratory, Los Alamos, NM, USA. [2]Lawrence Livermore National Laboratory, Livermore, CA, USA. ✉e-mail: anna_hayes@lanl.gov

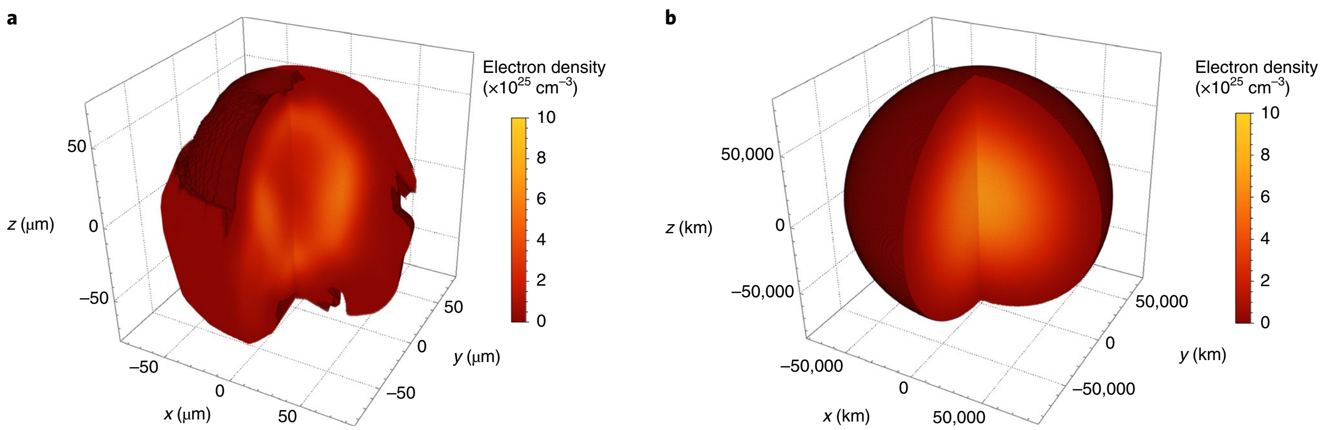

Fig. 1 | The density profiles for a NIF cryogenic capsule and astrophysical brown dwarfs are quite similar. The two systems also involve similar temperatures ($\theta \approx 0.2$ keV), and degrees of quantum degeneracy ($\psi \equiv \frac{E_F}{\theta}$). In general, NIF cryogenic cold fuels and low-mass brown dwarfs involve degeneracies in the range $\psi \approx 1-4$. **a**, The electron density deduced from neutron imaging of the imploded NIF cryogenic capsule N170328. The vertical axis is the polar direction. The lighter coloured region, which surrounds the central less-dense hotspot, corresponds to the cold fuel. The average electron density of the cold-fuel region is about 5×10^{25} cm^{-3}. The imploded capsule is not symmetric but the cold fuel is reasonably well formed. **b**, A simulated core density for a brown dwarf of mass $M = 0.05M_{\odot}$ and lifetime 0.1 Gyr.

change in the Debye radius leads to a suppression of the stopping power. This suppression enhances fluxes of energetic charged particles in the plasma, while a shift in the Bragg peak changes the shape of such fluxes. Observing these changes requires two diagnostics that probe above and below the Bragg peak.

There have been a number of earlier measurements on plasma stopping. For example, Evans et al.[18] measured the stopping of α-particles passing through laser-heated foils. Deutsch et al.[19] measured stopping well above the Bragg peak in non-degenerate plasmas, while Zylstra et al.[20] measured above the Bragg peak at a moderate degeneracy level ($\psi = \frac{E_F}{\theta} = 0.5$). Experiments by Frenje et al.[21] studied variations in the position of the Bragg peak in non-degenerate plasmas. In the last work, the Bragg peak dependence on the plasma average electron velocity was shown to be in good agreement with predictions[17].

The NIF ignition capsules used in the present experiments involve high-density carbon ablator designs[22,23] and CH ablator designs[24,25]. Capsules have three distinct material layers: an outer ablator layer, a thick layer of solid deuterium–tritium (DT) ice and a central sphere of DT gas. The designs chosen for this study generally show reasonable implosion symmetry and relatively high yields. The capsules are imploded along a low-entropy trajectory in pressure–density space to keep the ice layer as cold and dense as possible. This is to maximize the probability that the burn initiated in the central hotspot will propagate into the dense fuel and produce a high-gain yield[15]. The implosion adiabat, defined as the ratio of the pressure at peak implosion velocity to the Fermi pressure ($P_F = \frac{2}{5} n_e E_F$), is varied by changing the laser drive. Although the burn has not propagated into the cold fuels of cryogenic capsules to date, variations in the drive result in cold DT fuels with different electron densities that act as laboratories to study the effects of degeneracy on plasma properties, including stopping power.

Since the cold fuels in the NIF cryogenic capsules are not burning, and hence not producing any energetic ions, we carry out our studies using charged particles that are knocked up to megaelectronvolt energies by hotspot neutrons that are escaping the capsule. Some fraction of the knocked-on (KO) cold-fuel D and T ions undergo a DT reaction ($\mathrm{d} + \mathrm{t} \rightarrow \alpha + \mathrm{n}$) before losing their kinetic energy (Fig. 2). In this way, a spectrum of reaction-in-flight (RIF) neutrons with energies up to 30 MeV is produced, and these have been observed[26] in numerous NIF experiments. The KO ions are quickly slowed by

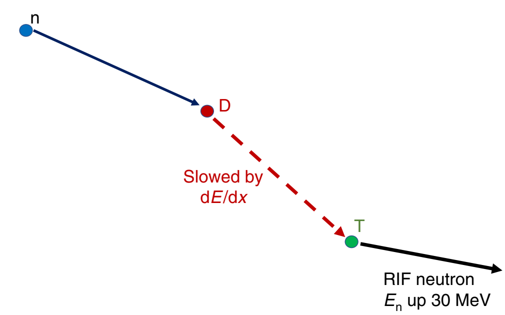

Fig. 2 | RIF production. RIF production in NIF capsules involves three consecutive steps. The figure displays this schematically. In the first step, a 14-MeV neutron (n) is produced in the capsule's central hotspot via a DT fusion reaction. This neutron can elastically scatter with D or T ions in the surrounding cold fuel, producing megaelectronvolt knock-on ions. The knock-on ion then undergoes a second DT fusion reaction in the cold fuel, producing a RIF neutron. The shape and magnitude of the RIF spectrum are determined by the stopping power ($\mathrm{d}E/\mathrm{d}x$) in this dense cold degenerate fuel.

the dense plasma and, as discussed in the Methods, this results in a KO fluence that is inversely proportional to the plasma stopping power. Thus, the shape and magnitude of the RIF spectrum reflect the stopping power[26,27], and we search for degeneracy-induced effects by measuring the RIF spectrum at two different energies.

In general, RIF spectra are 4–5 orders of magnitude in fluence below the primary 14-MeV neutron spectrum (Fig. 3b), making them very challenging to measure. The measurements are accomplished using a judicious choice of neutron activation foils that are placed outside the capsule target. For the lower-energy RIF measurement, we use the ^{169}Tm(n,3n)^{167}Tm reaction with a neutron threshold $E_n = 15$ MeV. To search for energy shifts in the Bragg peak, we use a second higher-energy RIF diagnostic foil, ^{209}Bi, and measure the ^{209}Bi(n,4n)^{206}Bi reaction with a threshold $E_n = 22.5$ MeV. For detection of the RIF-induced ^{206}Bi products in the irradiated Bi activation foils, a new clover detector has been installed at Lawrence Livermore National Laboratory, which is substantially equivalent to the Los Alamos clover detector used for the Tm measurements and described in ref. [26]. The experimental set-up for the foils in the

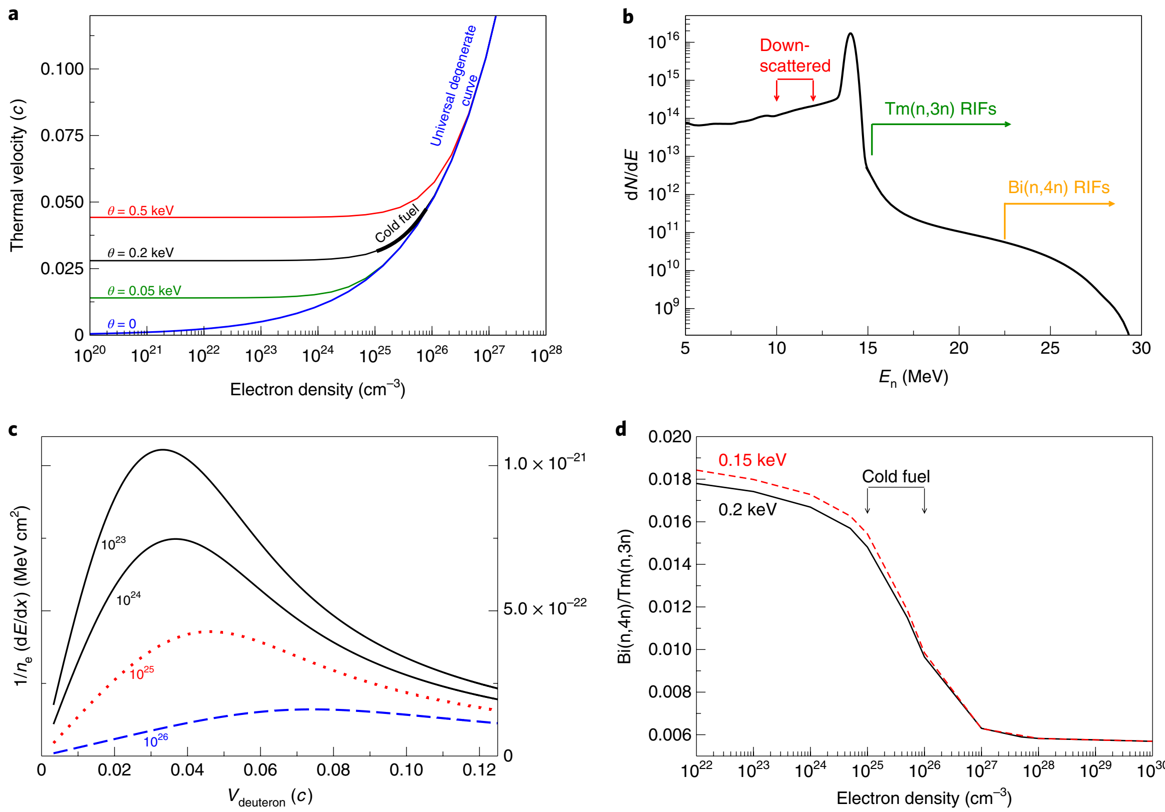

Fig. 3 | The effects of changes in the average electron velocity on the stopping power and RIF neutron spectra. The average electron velocity of the plasma determines the position of the Bragg peak in the stopping power, and the onset of degeneracy induces an increase in the average electron velocity, moving the Bragg peak to higher energies. This phenomenon can be probed by measuring the Tm(n,3n) and Bi(n,4n) reactions because these diagnostics probe the plasma stopping power above and below the Bragg peak. In particular, the Bi/Tm ratio drops by a factor of two in the transition region in response to this shift in the Bragg peak. **a**, The average electron velocities for different electron temperatures and densities. These curves were calculated using equation (1) in the Methods section. In non-degenerate plasmas, the average velocity is a function of temperature; in degenerate plasmas, it is a function of density. The cold fuel of NIF cryogenic capsules lies in the transition region between these two limits, where the average velocity is a function of both density and temperature. **b**, A simulated neutron spectrum for a typical NIF cryogenic capsule, indicating the energy regions probed by the Tm and Bi diagnostics. dN/dE is the number of neutrons per megaelectronvolt and E_n is the neutron energy. **c**, The calculated deuteron stopping power for an electron temperature of 0.2 keV and electron densities 10^{23}–10^{26} cm^{-3}. At densities above 10^{25} cm^{-3}, quantum degeneracy becomes important, causing the Bragg peak to move to higher deuteron energies. **d**, The expected degeneracy-induced decrease in the Bi/Tm ratio by about a factor of two over two orders of magnitude in density. This effect results from the shift in the Bragg peak. The red dashed curve was calculated assuming a plasma of temperature 0.15 keV and the solid black curve was calculated assuming a plasma of temperature 0.2 keV.

NIF chamber is also described in refs. [26,28], with the Tm and Bi foils placed back-to-back in the activation assembly. The Tm(n,3n) and Bi(n,4n) activation cross-sections were recently measured[29] and the corresponding average RIF neutron energies are $\langle E_n \rangle \approx 20$ MeV and $\langle E_n \rangle \approx 25$ MeV, respectively. Thus, we can use the ^{169}Tm(n,3n) reaction to determine the total number of RIFs produced above 15 MeV, and the ^{209}Bi(n,4n)/^{169}Tm(n,3n) ratio to measure the hardness of the RIF spectrum.

The uncertainty in the Bi/Tm measurements is dominated by uncertainties in fitting the γ-rays associated with the decays of ^{206}Bi and ^{167}Tm. In NIF shots with a 14-MeV yield of 10^{15} there are only about 2×10^4 atoms of ^{206}Bi produced and, thus, fitting the 803-keV γ-ray in the decay of ^{206}Bi dominates our experimental uncertainties. In general, this results in an uncertainly of about 12% in the determination of the Bi yield, when transposing the measured γ-ray intensity into the number of ^{206}Bi atoms produced. The uncertainties in the Tm signals are discussed in detail in ref. [26].

The capsules studied here are designed to form cold fuels with densities in the range 10^{25}–10^{26} cm^{-3}, and to have a temperature of about 0.2 keV. As shown in Fig. 3a, over this density range the average electron velocity increases by about 50%. The corresponding shift in the Bragg peak and the resulting drop in the Bi/Tm RIF ratio are significant (Fig. 3c,d). The last predictions are obtained using the Maynard–Deutsch[4] stopping-power model, which is a random-phase approximation model designed to handle arbitrary levels of degeneracy. Below about 10^{25} cm^{-3}, a plasma of temperature $\theta_e \approx 0.2$ keV is non-degenerate and both the Bragg peak and the Bi/Tm ratio vary only slowly, with the variation arising from the density dependence of the Coulomb logarithm. At very high densities ($n_e > 10^{27}$ cm^{-3}), where the system is fully degenerate, both the Bi and Tm diagnostics probe dE/dx below the Bragg peak, and the Bi/Tm ratio no longer changes significantly with density. Thus, there is a relatively small range in density that is ideal for probing partial quantum degeneracy via RIF neutrons, and this is the same as the window scanned by the NIF experiments.

The electron density of the cold fuel is not measured directly, and we need to deduce it from other observables. The temperature of the cold fuel is also not measured, but the signature for the transition to quantum degeneracy is only slightly dependent on temperature (Fig. 3d). This is because the stopping power is dominated by an effective temperature that is determined by the Fermi energy. As we discuss in the Methods, the total number of RIFs per unit

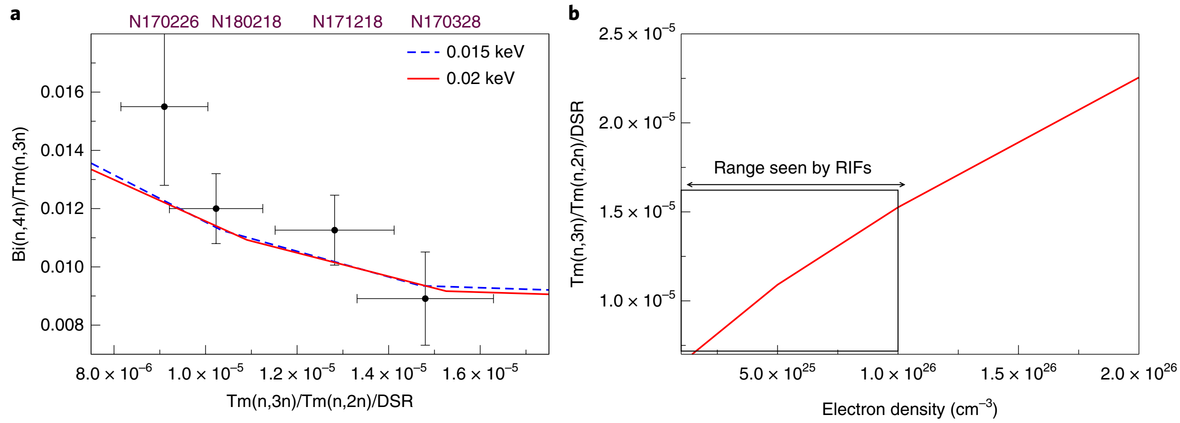

Fig. 4 | The experimental data as a function of the surrogate for the electron density. The Bi/Tm ratio measures the hardness of the RIF neutron spectra. This ratio is observed to decease by a factor of two with increasing electron density. **a**, The measured Bi/Tm RIF ratios, which represent the ratio of RIF neutrons at neutron energy $E_n \approx$ <25 MeV> to those at neutron energy $E_n \approx$ <20 MeV>, as a function of the surrogate for the cold-fuel density. The uncertainties for the data shown are at the 1σ level. The uncertainties include γ-ray detection efficiency, γ-ray branching ratios and counting statistics; the square root of a sum of squares. There is no correlation between Bi and Tm γ-ray efficiencies as two independent detector systems were used. The two curves are the expected Bi/Tm ratios for the electron temperatures indicated. The numbers at the top of the graph (N170226, N180218 and so on) indicate the NIF shot number. **b**, The line shows the scaling of the calculated surrogate ratio with electron density. Here Tm(n,3n) is a measure of the total number of RIF neutrons, Tm(n,2n) is a measure of the 14-MeV neutron yield of the imploded capsule and DSR is a measure of the cold-fuel areal density. The deviation from a straight line at lower densities occurs because the system is only partially degenerate in this region.

areal density per 14-MeV neutron is directly proportional to the electron density; that is, $n_e \propto \frac{N_{\mathrm{RIF}}}{<\rho r> N_{14}}$. To obtain this ratio from our measurements, we use the equivalent ratio Tm(n,3n)/(Tm(n,2n) DSR) as a surrogate for n_e. Here Tm(n,2n), the number of ^{168}Tm atoms produced, measures the number of 14-MeV neutrons reaching the Tm foil, and the down-scatter ratio (DSR), which is the ratio of 10–12 MeV to 13–15 MeV neutrons, is a measure of the cold-fuel areal density[30]. Since the imploded cold fuels can be asymmetric, we use the average DSR measured in the direction of the Tm and Bi foils to calculate the surrogate for the electron density.

In Fig. 4a, we show the measured Bi/Tm RIF ratios as a function of the surrogate for the electron density. The RIF ratio is found to drop with increasing density, so that the hardness of the RIF spectra inversely correlates with the degree of degeneracy. Using a simple linear model to describe the variation of the Bi/Tm ratio as a function of the electron-density surrogate, we find that the observed decrease supports the existence of a shift in the position of the Bragg peak at the 90% confidence level. The data cannot discriminate between a linear drop in Bi/Tm versus the theoretical curves of Fig. 4a, but they do discriminate between a linear approximation to theory and no change in the RIF ratio at the quoted 90% level. The shift in the Bi/Tm ratio also occurs over the range in the electron density where the transition is expected to occur. Figure 3d shows that for a non-degenerate plasma, the Bi/Tm ratio would always remain above the maximum observed value of 0.016; for a fully degenerate plasma, the ratio would stay near the minimum of 0.009. Instead, the observed ratios span the gap between these limits and the data rule out a purely non-degenerate or purely degenerate plasma with 3σ confidence. In addition, the total magnitude of the RIF production, as measured by the Tm(n,3n) per 14-MeV neutron signal, is enhanced[26] by a factor of about 1.5 compared to what would be expected if the plasma were non-degenerate. The opposite limit of a fully degenerate plasma corresponds to an electron density exceeding 10^{26} electrons cm^{-3}, which would correspond to a considerably higher compression than has ever been achieved at NIF. Thus, we find that our RIF data, which represent measurements of the shape of such spectra in inertial confinement fusion plasmas, provide evidence for a shift of the Bragg peak to higher energies with increasing degeneracy, which is the expected signature for an increase in the plasma average electron velocity with density, as well as consistency with the overall production rate and therefore with the predictions for the Coulomb logarithm in this regime.

Confirmation of the inverse correlation between the hardness of the RIF spectra and the cold-fuel electron density is provided by neutron imaging data. The down-scattered neutrons in the energy window 6–12 MeV are used to image the cold fuel to 10-μm resolution using a pinhole neutron aperture, placed between the capsule and a neutron detector[31]. The two-dimensional distribution of neutrons passing through the pinholes is converted into a density image of the cold fuel, using a second image of the neutron source via gating between 13 and 17 MeV. This technique was used to generate the density image of the NIF capsule shown in Fig. 1. We find that the lower Bi/Tm ratios are correlated with well-formed and reasonably symmetric cold fuels, whereas high Bi/Tm ratios are correlated with less well-formed cold fuels. In Fig. 5 we show the neutron imaging data for shots N170226 and N170328. The correlation seen between lower-density cold-fuel images and harder RIF spectra is consistent with the fact that we also measure fewer total RIFs per 14-MeV neutron as the spectra get harder. Additional evidence for the higher compression reached by the N170328[24,25] CH design is provided by its measured DSR value (~3:6%), compared to that for the high-density carbon N170226 design (DSR ≈ 2:82%)[22,23].

The cold-fuel electron-density surrogate used in Fig. 4 can be interpreted only as an average density because there is not one single density associated with the dense non-burning plasmas surrounding the hotspot. Both neutron images of the cold fuel and measurements of the DSRs at different three-dimensional positions around the NIF chamber show evidence of cold-fuel asymmetries. When such data suggest very large asymmetries, the RIF data tend not to follow the systematic trends discussed throughout this work. As an example, the NIF shot N160509, which was a so-called high-foot design[32], used a DT fill tube that was three times thicker than normal, was measured to be unusually asymmetric and the measured RIF data proved difficult to interpret. Other shots also show very asymmetric implosion, wherein the thickness of the cold fuel in the polar direction is considerably larger than in the equatorial direction. For the current analysis, we restrict ourselves to NIF cryogenic shots that involve reasonably symmetric implosions.

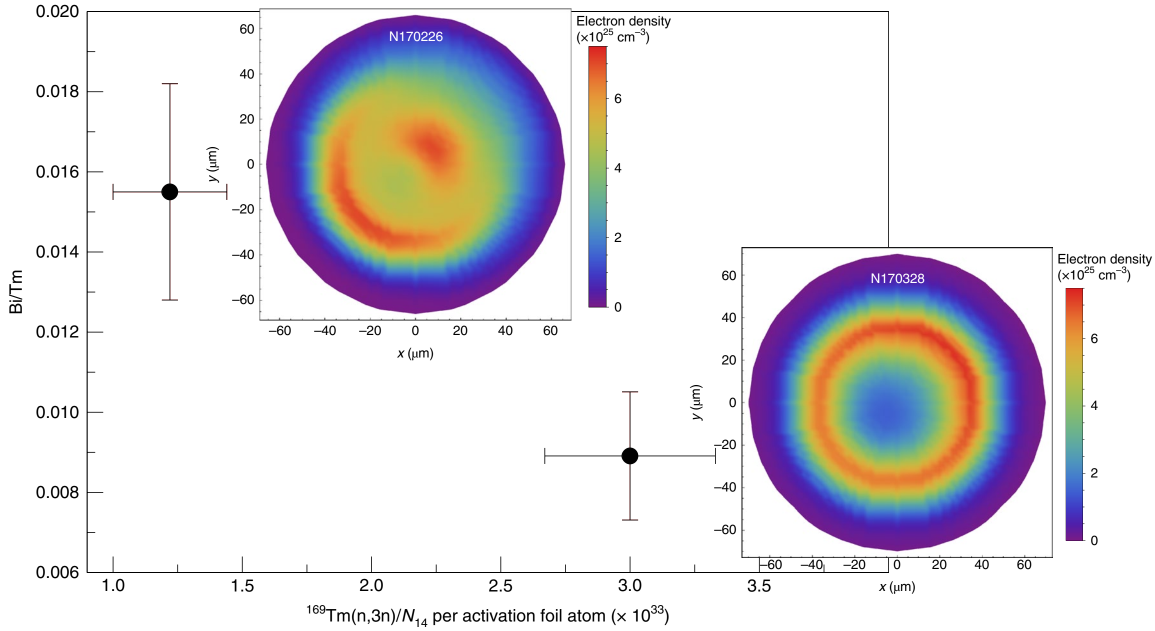

Fig. 5 | Neutron images for two shots, together with corresponding RIF data. We find a correlation between the RIF ratios and the neutron images for shots. For example, comparing shots N170226 and N170328, the better formed and more dense cold fuel of shot N170328 produced more RIFs per 14-MeV neutron yield, but a softer RIF spectrum. These neutron images are looking down from the polar direction. The uncertainties for the Bi and Tm data points (black) represent the 1σ level. As in the case of Fig. 4, they include γ-ray detection efficiency, γ-ray branching ratios and counting statistics; the square root of a sum of squares.

In the case of approximately symmetric implosions, the RIF data demonstrate that the cold-fuel stopping powers reflect variations in electron quantum degeneracy from shot to shot. We observe two changes in the RIF spectra: an enhancement in the total RIF production arising from a change in the Debye radius that controls the Coulomb logarithm of the stopping power; and a softening of the RIF spectra from a shift of the Bragg peak to higher energies with increasing degeneracy. The change in the Debye radius, equation (2) in the Methods, is predicted[2,5,33–35] to be the main effect on Coulomb screening of thermonuclear reactions induced by quantum degeneracy. In this sense, our RIF data support the screening models used for partially degenerate astrophysical systems, such as brown dwarfs. This in turn affects the viability of D fusion taking place in brown dwarfs, although other physics, such as the equation of state, also play important roles in determining the brown dwarf fusion rates. The observed shift in the Bragg peak emphasizes the importance of Fermi–Dirac statistics in the description of the transport properties of partially degeneracy systems. Over the lifetime of a 0.05 $M_{\odot}$ brown dwarf, the degree of degeneracy steadily increases, and spans a similar degeneracy range to the cold fuels formed at NIF. New cryogenic capsule designs and laser drives are continually being tested at NIF, so that the degree of partial degeneracy could eventually be varied over a broader range than is studied here. As the total DT yields of NIF cryogenic capsules increase, the uncertainties in the RIF diagnostics will decrease, allowing higher-precision studies of degenerate stopping powers.

Online content

Any methods, additional references, Nature Research reporting summaries, source data, extended data, supplementary information, acknowledgements, peer review information; details of author contributions and competing interests; and statements of data and code availability are available at https://doi.org/10.1038/s41567-020-0790-3.

Received: 28 March 2019; Accepted: 7 January 2020;
Published online: 9 March 2020

References

1. Daligault, J. Crossover from classical to Fermi liquid behavior in dense plasmas. *Phys. Rev. Lett.* **119**, 045002 (2017).
2. Salpeter, E. E. Electron screening and thermonuclear reaction rates. *Aust. J. Phys.* **7**, 373–388 (1954).
3. Shternin, P. S. Shear viscosity of degenerate electron matter. *J. Phys. A* **41**, 205501 (2008).
4. Maynard, G. & Deutsch, C. Born random phase approximation for ion stopping in an arbitrarily degenerate electron fluid. *J. Phys.* **46**, 1113–1122 (1985).
5. Skupsky, S. Energy loss of ions moving through high-density matter. *Phys. Rev. A* **16**, 727–731 (1977).
6. Dar, A., Grunzweig-Genossar, J., Peres, A., Revzen, M. & Rob, A. Slowing down of ions by ultrahigh-density electron plasma. *Phys. Rev. Lett.* **32**, 1299–1301 (1974).
7. Li, C. & Pettrasso, R. D. Effects of scattering upon energetic ion energy loss in plasmas. *Phys. Plasma* **2**, 2460–2464 (1995).
8. Brown, L. S. & Singleton, R. L. Jr Temperature equilibration rate with Fermi–Dirac statistics. *Phys. Rev. E* **76**, 066404 (2007).
9. Lee, Y. T. & More, R. M. An electron conductivity model for dense plasmas. *Phys. Fluids* **27**, 1273–1286 (1984).
10. Longair, M. S. *The Cosmic Century: A History of Astrophysics and Cosmology* (Cambridge Univ. Press, 2006).
11. Marshak, R. E. The internal temperature of white dwarf stars. *Astrophys. J.* **92**, 321–353 (1940).
12. Lattimer, J. M. & Prakash, M. The physics of neutron stars. *Science* **304**, 536–542 (2004).
13. Ashcroft, N. W. & Mermin, N. D. *Solid State Physics* (Harcourt School, 1987).
14. Burrows, A. & Liebert, J. The science of brown dwarfs. *Rev. Mod. Phys.* **65**, 301–336 (1993).
15. Lindl, J. Development of the indirect-drive approach to inertial confinement fusion and the target physics basis for ignition and gain. *Phys. Plasmas* **2**, 3933–4024 (1995).
16. Edwards, M. J. et al. Progress towards ignition on the National Ignition Facility. *Phys. Plasmas* **20**, 070501 (2013).
17. Brown, L. S., Preston, D. L. & Singleton, R. L. Jr Charged particle motion in a highly ionized plasma. *Phys. Rep.* **410**, 237–333 (2005).
18. Evans, P. M., Fews, A. P. & Toner, W. T. Diagnosis of laser produced plasmas using fusion reaction products. *Laser Part. Beams* **6**, 353–360 (1988).

19. Deutsch, C. & Maynard, G. et al. Ion stopping in dense plasma target for high energy density physics. *Open Plasma Phys. J.* **3**, 88–115 (2010).
20. Zylstra, A. B. et al. Measurements of charged-particle stopping in warm dense plasma. *Phys. Rev.* **114**, 215002 (2015).
21. Frenje, J. A. et al. Measurements of ion stopping around the Bragg peak in high-energy-density plasmas. *Phys. Rev. Lett.* **115**, 205001 (2015).
22. Hopkins, L. Berzak et al. Increasing stagnation pressure and thermonuclear performance of inertial confinement fusion capsules by the introduction of a high-Z dopant. *Phys. Plasmas* **25**, 080706 (2018).
23. Divol, L. et al. Symmetry control of an indirectly driven high-density-carbon implosion at high convergence and high velocity. *Phys. Plasmas* **24**, 056309 (2017).
24. Hinkel, D. E. et al. Development of improved radiation drive environment for high foot implosions at the National Ignition Facility. *Phys. Rev. Lett.* **117**, 225002 (2016).
25. Hinkel, D. E. et al. Publisher's note: development of improved radiation drive environment for high foot implosions at the National Ignition Facility. *Phys. Rev. Lett.* **118**, 089902 (2017).
26. Hayes, A. C. et al. Reaction-in-flight neutrons as a test of stopping power in degenerate plasmas. *Phys. Plasmas* **22**, 082703 (2015).
27. Hayes, A. C., Bradley, P. A., Grim, G. P., Jungman, G. & Wilhelmy, J. B. Reaction-in-flight neutrons as a signature for shell mixing in National Ignition Facility capsules. *Phys. Plasmas* **17**, 012705 (2010).
28. Hayes, A. C. et al. Reaction-in-flight neutrons as a test of stopping power in degenerate plasmas. *J. Phys. Conf. Ser.* **717**, 012022 (2016).
29. Gooden, M. E. et al. Measurement of the ^{209}Bi$(n,4n)$ ^{206}Bi and ^{169}Tm$(n,3n)$ ^{167}Tm cross sections between 23.5 and 30.5 MeV relevant to reaction-in-flight neutron studies at the National Ignition Facility. *Phys. Rev. C* **96**, 024622 (2017).
30. GatuJohnson, M. M. et al. Neutron spectrometry–an essential tool for diagnosing implosions at the National Ignition Facility. *Rev. Sci. Instrum.* **83**, 10D308 (2012).
31. Merrill, F. E. et al. The neutron imaging diagnostic at NIF. *Rev. Sci. Instrum.* **83**, 10D317 (2012).
32. Hurricane, O. A. et al. The high-foot implosion campaign on the National Ignition Facility. *Phys. Plasmas* **21**, 056314 (2014).
33. Salpeter, E. E. & Van Horn, H. M. Nuclear reaction rates at high density. *Astrophys. J.* **155**, 183–202 (1969).
34. DeWitt, H. E., Graboske, H. C. & Cooper, M. S. Screening factors for nuclear reaction. I General theory. *Astrophys. J.* **181**, 439–456 (1973).
35. Graboske, H. C., DeWitt, H. E., Grossman, A. S. & Cooper, M. S. Screening factors for nuclear reactions. II Intermediate screening and astrophysical applications. *Astrophys. J.* **181**, 457–474 (1973).

Methods

The definition of the average electron velocity in non-degenerate systems used throughout the current work ($v_{avg} = \sqrt{2\theta_e/m_e}$) differs from that used in ref. [17], where $v_{avg} = \sqrt{3\theta_e/m_e}$. However, this difference in definitions has no effect on any of the conclusions found here. The expression for the average electron velocity for non-degenerate plasmas can be generalized to the degenerate or partially degenerate case by introducing an effective temperature, with $v_{avg} \equiv \sqrt{2\theta_{eff}/m_e}$. For any degeneracy, the average velocity becomes[4,5,36]

$$v_{avg} = \sqrt{\frac{2\theta}{m_e}}\left[\frac{2}{\sqrt{\pi}}F_{1/2}(\eta)(1+e^{-\eta})\right]^{1/3} \quad (1)$$

where $F_{1/2}(\eta) = \int_0^\infty x^{1/2}(e^{x-\eta}+1)^{-1}dx$ and $\eta = \mu/\theta$, and μ is the chemical potential. Equation (1) is used in the top left panel of Fig. 3, and has the following limiting values:

$$\eta \to -\infty \quad \text{as} \quad \theta_{eff} \to \theta$$

$$\eta \to +\infty \quad \text{as} \quad \theta_{eff} \to \left(\frac{4}{3\sqrt{\pi}}\right)^{\frac{2}{3}} E_F$$

In addition to the change in the average electron velocity, there is a degeneracy-induced change in the Coulomb logarithm entering the plasma stopping power. This is exactly analogous to the degeneracy-induced change in the radius controlling screening of thermonuclear reactions in brown dwarfs. In both cases, the change enters through a change in the Debye wavenumber[2,5]

$$k_D^2 \to k_D^2 F'_{1/2}(\eta)/F_{1/2}(\eta) \quad (2)$$

where the Debye wavenumber, which is the inverse of the Debye radius, is

$$k_D = \sqrt{\frac{4\pi n e^2}{\theta}}$$

The detector systems used for these measurements consist of two high-efficiency clover Ge detectors. Each clover involves four segmented high-purity Ge crystals, surrounded by an active NaI Compton suppressor. ^{167}Tm decays to a 208-keV isomeric level in ^{167}Er that has a half-life of 2.28 s. This level decays 100% of the time to the ^{167}Er ground state. ^{206}Bi decays with a half-life of 6.243 d, producing an 803-keV γ-ray. In several shots, two Bi foils were assayed using both a clover detector and a second detector known as BIG 8. Consistency between the assays made with these two independent detectors provides confidence in the measurements.

The RIF spectrum per unit volume is determined by the KO fluence and is given by

$$\frac{1}{dV}\frac{dN_{RIF}}{dE_{RIF}} = n_d \int \frac{d\psi_{ko}^t}{dE_{ko}}\sigma_{dt}\frac{dF}{dE_{RIF}}dE_{ko} + n_t \int \frac{d\psi_{ko}^d}{dE_{ko}}\sigma_{dt}\frac{dF}{dE_{RIF}}dE_{ko} \quad (3)$$

where $n_d(n_t)$ is the density of deuterons (tritons) in the cold fuel, σ_{dt} is the DT cross-section and dF/dE_{RIF} is the kinematic weight for producing a RIF neutron of energy E_{RIF} from a KO ion of energy E_{ko}. The KO fluence $d\psi_{ko}dE_{ko}$ is inversely related to the stopping power by[37]

$$\frac{d\psi_{ko}^{d(t)}}{dE_{ko}} = \frac{\Phi_n n_{d(t)}\sigma_{ko}}{|dE/dx(E_{ko})|}\int_{E_{ko}}^{\infty} dE_0 q(E_0), \quad (4)$$

where Φ_n is the neutron fluence, $n_{d(t)}$ is the density of D or T ions in the cold fuel, σ_{ko} is the knock-on cross-section and $q(E_0)$ is the initial KO spectrum before transport.

The stopping power can be written

$$\frac{dE}{dx} = -\sqrt{E}\frac{8\sqrt{\pi}Z^2e^4}{3}\frac{n_e}{\theta_{eff}^{3/2}}\left(\frac{m_e}{M_{ko}}\right)^{1/2}\ln\Lambda \times f\left(\frac{v}{v_{avg}}\right) \quad (5)$$

where $\ln\Lambda$ is the Coulomb logarithm, θ_{eff} is defined by equation (1) and $f(\frac{v}{v_{avg}})$ is short-hand for the dependence on the dimensionless velocity ratio. In the absence of hydrodynamical mixing of the ablator into the cold fuel, $n_e = n_{dt}$, where n_{dt} is the density of D and T ions. Thus, for $Z = 1$ projectiles, the stopping power scales with the cold-fuel density and effective temperature as

$$\frac{dE}{dx} \propto \frac{n_{d(t)}\sqrt{E}}{\theta_{eff}^{3/2}}$$

Here θ_{eff} is the effective temperature, which for a degenerate plasma, is proportional to the Fermi energy, so that $\theta_{eff}^{3/2} \propto n_e$ for complete degeneracy. The neutron fluence in the cold fuel falls off approximately inversely with distance, $\Phi_n = N_{14}/4\pi r^2$. Thus, for a degenerate plasma, the total number of RIF neutrons scales with the 14-MeV neutron yield (N_{14}), the areal density of the cold fuel, $<\rho r>$, and the cold-fuel electron density

$$N_{RIF} \propto N_{14}\langle \rho r\rangle n_e$$

Tm(n,3n) (Tm(n,2n)) is a measure of the total number of RIF (14-MeV) neutrons and the DSR is a measure of $<\rho r>$. Thus, the ratio of observables Tm(n,3n)/(Tm(n,2n)DSR) can be used as a surrogate for the electron density, and the scaling is as shown in the right side of Fig. 4. We note that the Tm(n,2n) diagnostic is directly correlated with all of the other NIF neutron activation diagnostics for 14-MeV neutrons.

Data availability

Source data for Figs. 3 and 4 are available with the paper. All other data that support the plots within this paper and other findings of this study are available from the corresponding author upon reasonable request.

References

36. Zimmerman, G. B. *Recent Developments in Monte Carlo* Report No. UCRL-JC-105616 (Lawrence Livermore National Laboratory, 1990).
37. Jungman, G. & Hayes, A. C. *The Relationship between Charged-Particle Fluence and Stopping Power* Report No. LA-UR-13-26171 (Los Alamos National Laboratory, 2013).

Author contributions

A.C.H. was the RIF campaign lead and conducted theoretical data analysis. M.E.G. took RIF measurements. E.H. took RIF measurements. G.J. conducted theoretical analysis. J.B.W. conducted data analysis. R.S.R. took RIF measurements and conducted detector design. C.Y. conducted activation diagnostic analysis. G.K. conducted data analysis. C.C. performed hydrodynamical simulations. D.L.D. performed brown dwarf simulations, conducted data analysis and prepared graphics. J.D. conducted theoretical analysis. C. Wilburn conducted data analysis and prepared graphics. P.V. conducted neutron imaging. C. Wilde conducted neutron imaging. S.B. undertook experimental planning and design. T.B. was responsible for detector installation. J.L.K. conducted experimental planning. G.P.G. conducted neutron time-of-flight analysis. E.P.H. conducted neutron time-of-flight analysis. D. Shaughnessy conducted data analysis. C.V. took part in experimental discussions. W.S.C. took part in experimental discussions. K. Moody conducted data collection and analysis. L.F.B.H. undertook capsule design and simulations. D.H. undertook capsule design and simulations. T.D. undertook experimental design and planning. S.L.P. undertook experimental design and planning. F.G. conducted theoretical analysis. D.A.C. undertook capsule design and simulations. O.A.H. undertook capsule design and simulations. D. Schneider conducted experimental design.

Competing interests

The authors declare no competing interests.

Additional information

Supplementary information is available for this paper at https://doi.org/10.1038/s41567-020-0790-3.

Correspondence and requests for materials should be addressed to A.C.H.

Peer review information *Nature Physics* thanks Adam Burgasser, Giovanni Manfredi and Peter Norreys for their contribution to the peer review of this work.

Reprints and permissions information is available at www.nature.com/reprints.